minerals

MDPI

Article

Acoustic Emission-Based Modeling of Fiber Tailings Cementation and Filling Body Dynamics and Damage Ontology

Chunlei Zhang [1,2], Xuelin Song [1,2], Yuhua Fu [1,2,3,*], Daxing Lei [3], Weijie She [1] and Wenxiao Zhu [1]

[1] School of Resources and Environmental Engineering, Jiangxi University of Science and Technology, Ganzhou 341000, China; sxl07071997@126.com (X.S.)
[2] Jiangxi Key Laboratory of Mining Engineering, Jiangxi University of Science and Technology, Ganzhou 341000, China
[3] School of Resource and Construction Engineering, Gannan University of Science and Technology, Ganzhou 341000, China
* Correspondence: fyh1369@126.com

Abstract: Optimizing the mechanical characteristics of cemented tailings backfill (CTB) and quickly identifying its damage state under external loading, this study compares and prepares CTB specimens without fiber, doped with polypropylene fiber (PF), doped with glass fiber (BL), and doped with polypropylene and glass blended fiber (PB). Uniaxial compression and acoustic emission (AE) monitoring experiments are also conducted. Based on the cumulative energy of AE, the damage ontology model of CTB was developed. As shown by the study's findings, adding various fibers can greatly enhance the filler body's uniaxial compressive strength (UCS). BL has the greatest effect, followed by PB, while PFs have the least effect. Furthermore, the fibers primarily prevent the growth of crack extension by extending or breaking themselves, The results of the tests on acoustic emission revealed that the fiberless filler's signals were more active prior to the peak point and less intense in the later stages of the damage, whereas the fiber-doped filler's signals began to increase following the peak point and remained high. Thus, the damage model curves of various fiber-filled bodies are constructed based on the cumulative energy of acoustic emission, and the experimental data verification shows that the two have good consistency, suggesting that the established theoretical model can serve as a basis of reference for assessing the filled bodies' damage state.

Keywords: mechanical characteristics; damage state; fiber; uniaxial compression; AE monitoring

check for updates

Citation: Zhang, C.; Song, X.; Fu, Y.; Lei, D.; She, W.; Zhu, W. Acoustic Emission-Based Modeling of Fiber Tailings Cementation and Filling Body Dynamics and Damage Ontology. *Minerals* **2023**, *13*, 1499. https://doi.org/10.3390/min13121499

Academic Editor: Elsabe Kearsley

Received: 9 November 2023
Revised: 24 November 2023
Accepted: 25 November 2023
Published: 29 November 2023

Copyright: © 2023 by the authors. Licensee MDPI, Basel, Switzerland. This article is an open access article distributed under the terms and conditions of the Creative Commons Attribution (CC BY) license (https://creativecommons.org/licenses/by/4.0/).

1. Introduction

As mining continues to advance to greater depths, infill mining is widely used because of its unique advantages. However, "three highs and one disturbance" and other issues that impact the stability of CTB are inevitable with deep mining [1–3]. Therefore, in order to reduce the risk of mining accidents and disasters, it is essential to improve CTB's mechanical features in the difficult deep environment and to promptly monitor its damage state. It has been shown that improving the mechanical characteristics of CTB by adding a sufficient amount of fibers to the filling slurry can prevent the thorough development of cracks after CTB is loaded [4,5]. Additionally, AE can track the growth and expansion of fractures inside CTB over time as a non-destructive monitoring method, revealing the internal damage state of CTB [6,7].

Currently, a great deal of domestic and international research has been conducted on the effects of fibers on filling body mechanical qualities and acoustic emission properties. For example, by conducting uniaxial compression tests on fillers doped with various fibers, Cao [8] investigated the mechanism through which the fibers influence the fillers' early toughness and strength changes. By varying the length and number of polypropylene fibers in Brazilian splitting experiments on paste fillers, Chen [9] investigated the causes of the increase in filler tensile strength brought on by polypropylene fibers. With fiber length

as the variable, Xue [10] performed uniaxial compression studies on fillers of various sizes and examined the reasons why cubic-shaped fillers had superior mechanical properties to cylindrical ones. Zhao Kang [11] studied the early mechanical characteristics of several fiber-tailing-containing cement fillers and created a damage ontology model for these fillers. Microscopically analyzing the reinforcing process of straw fibers, Ruan Zhu'en [12] performed uniaxial compression tests on sulfur-containing tailing sand-cemented filler. To define the mechanism of filler damage development based on energy evolution, Song [13] conducted uniaxial compression experiments on tailing sand-cemented fillers containing straw fibers. Wang [14] performed uniaxial compression acoustic emission experiments on layered paste fillers with various structural characteristics, examined the mechanical behavior and acoustic emission properties of layered paste fillers, and created a damage model based on the strain equivalence assumption and the Newtonian body assumption. Sun [15] conducted uniaxial compression acoustic emission tests on gangue-doped and high-water-content material-cemented paste filler, analyzed its damage and acoustic emission characteristics, and created damage constitutive equations based on cumulative counts of acoustic emission. Cheng [16] examined the filled body's acoustic emission properties under uniaxial compression. Based on particle flow and moment tensor theories, he created a fine-scale model of the filled body's acoustic emission, which disclosed the filled body's rupture process. Xia Yu [17] performed uniaxial compression acoustic emission tests on filling bodies with various aggregate particle sizes and used Tepo index analysis to determine the filling body mechanical behavior variation rules. Zhao Kang [18,19] examined the fracture evolution features of filled solids under uniaxial compression and discovered an inherent relationship between crack kinds and acoustic emission parameters.

Based on the above studies, it can be seen that the incorporation of an appropriate amount of fiber can significantly improve the mechanical characteristics of CTB so that it can better play a role in the downhole. In addition, the AE signals can effectively reflect the degree of crack growth and expansion of CTB in the process of destruction, allowing a characterization of the damage state of CTB [20,21]. To advance the use of fiber-reinforced technology in the mining industry, it is urgently necessary to enrich the evolution of the AE signals of various fiber fillers during the damage process. This is because the mechanical behavior and AE characteristics of various fiber fillers during uniaxial compression are still poorly understood.

Using this information as a foundation, this study suggests conducting uniaxial compression AE experiments on fillers doped with various fibers to examine how these fibers affect the fillers' strength, damage modes, and AE characteristics. It also proposes developing and validating a damage intrinsic model for fillers doped with various fibers based on the cumulative energy of AE.

2. Experimental Materials and Methods

2.1. Raw Materials

The particle size distribution and physicochemical makeup of the tailing sand utilized in the experiment, which was obtained from a mine in the Fujian Province, are displayed in Figure 1 and Table 1. It can be determined from Figure 1 that the tailing sand has poor grading since d_{10} = 3.14 μm, d_{30} = 7.6 μm, d_{50} = 14.9 μm, d_{60} = 19.8 μm, $Cu(d_{60}/d_{10})$ = 6.3, and $Cc(d_{30}^2/d_{60} \times d_{10})$ = 0.93. According to Table 1, the amounts of SiO_2, CaO, MgO, and Al_2O_3 in the tailing sand's total mass were 39.21%, 23.24%, 8.20%, and 4.22%, respectively. Based to the acid–base formula, $M_0 = (CaO + MgO)/(SiO_2 + Al_2O_3) = 0.724 < 1$, meaning the mine belongs to the acidic tailing. The chemical makeup of the cementitious material employed in the experiment, common silicate cement (P.O42.5R), is displayed in Table 2. Table 3 lists the key physical and mechanical performance metrics for the experiment's polypropylene and glass fibers, both of which were produced in Jinan, Shandong Province. Water from the tap was used in the experiment.

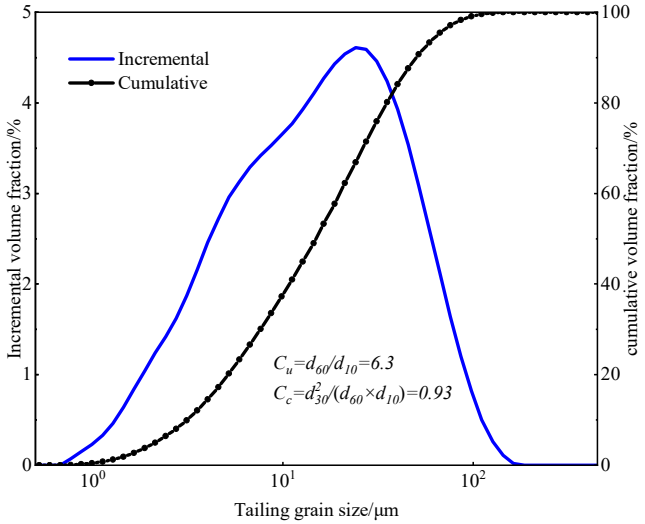


Figure 1. Tailings particle size distribution.

Table 1. Chemical composition of tailings (mass fraction,%).

SiO_2	CaO	Fe_2O_3	MgO	Al_2O_3	MnO	F	SO_3	K_2O	TiO_2
39.21	23.24	14.23	8.20	4.22	1.92	1.07	0.53	0.40	0.20

Table 2. Chemical composition of cement (%).

Al_2O_3	CaO	SiO_2	Fe_2O_3	SO_3	MgO
8.26	51.42	24.99	4.03	2.51	3.71

Table 3. Main physico-mechanical property parameters of the fibers.

Fiber Type	Lengths/mm	Densities/ $g\cdot cm^{-3}$	Tensile Strength/MPa	Modulus of Elasticity/GPa	Elongation at Break/%	Geometry
PF	12	0.91	450	3.64	29.5	orbicular
BL	12	0.91	369	5.2	36.4	orbicular

2.2. Specimen Preparation

Following the pre-test and in conjunction with the mine's actual conditions, this paper followed the grey to sand ratio of 1:4, slurry mass fraction of 75% of CTB experimental ratios, and the same level of configuration for the three groups of specimens. The preparation of the fiber doping for the dry tailing sand and cement accounted for 0.6% of the total mass of the fiber doping. Mixed fiber doping accounted for 0.3%. Due to the lightness of the fiber, it is simple for it to float on the slurry's surface during the slurry preparation process, resulting in an uneven distribution of fiber in the filling matrix. To combat this phenomenon, the technique of "dry mixing first" and "wet mixing again" was adopted, and the slurry was injected into a 50 × 100 mm round mold after being evenly mixed. After 24 h, the mold was taken out and placed in a curing box with a consistent temperature and humidity for 7 days. When the maintenance was finished, a WDW-20 electronic universal testing machine was used for loading with a loading rate of 0.5 mm/min. The American Physical Acoustics Company's AE monitoring system was used for signal acquisition. This system's main components were R6 sensors, preamplifiers, PCI-II AE meters, control computers, and the AEwin software system. The specific test process is shown in Figure 2.

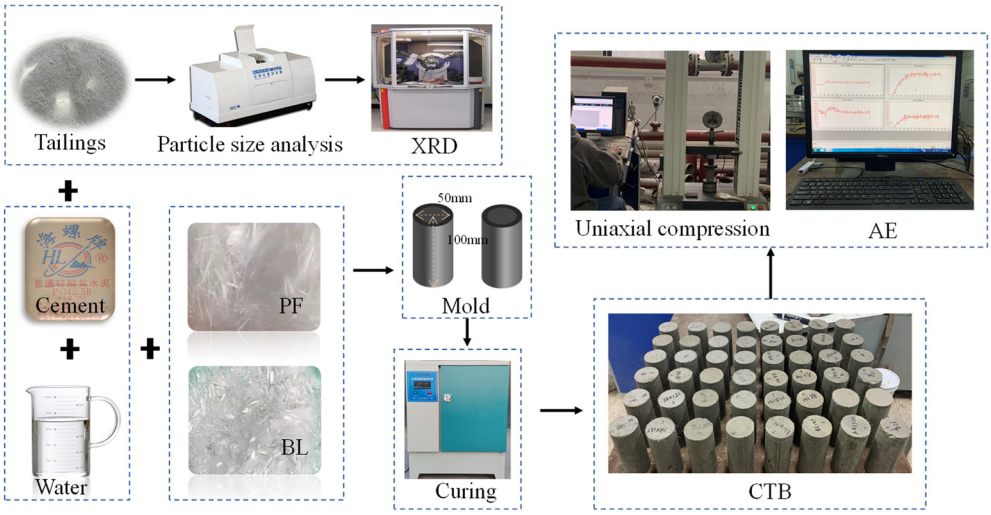


Figure 2. Flow chart of the test process.

3. Analysis of Test Results

3.1. Analysis of Fiber Influence on the Strength of the Filling Body

To examine the impact of adding PF, BL, or PB on the filling body's uniaxial compressive strength, the three horizontal specimens in each group had their uniaxial compressive strengths computed statistically and averaged, as illustrated in Figure 3. Figure 3 shows that the fiber-free CTB, the PF-CTB, the BL-CTB, and the PB-CTB had respective uniaxial compressive strengths of 2.39, 2.55, 2.72, and 2.63 MPa. Comparing the uniaxial compressive strengths of the fiber-free CTB, the uniaxial compressive strengths of the PF, BL, and PB increased by 6.69%, 13.81%, and 10.04%, respectively. This finding demonstrates that BL reinforcement was the most effective, followed by PB, and PF was the least effective.

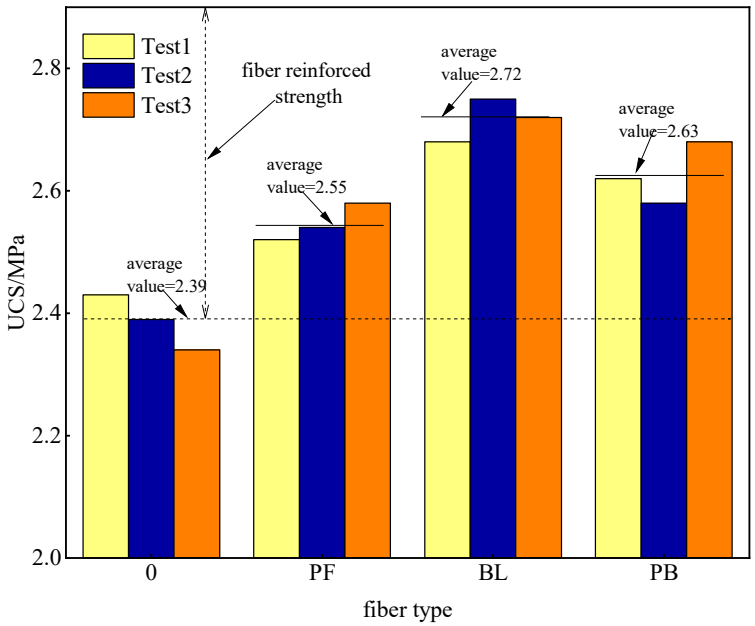


Figure 3. Uniaxial compressive strength of fillers with different fibers.

When the filled body is subjected to external load that causes internal cracks to sprout, the BL in the matrix prevent the cracks from expanding, highlighting the role of the linkage. This stress transfer accounted for the better performance ratio of BL compared to PF or PB. This is why the uniaxial compressive strength of the filled body exhibits different increase

patterns due to different doped fibers. The main reason is that BL has a greater modulus of elasticity and a higher elongation at break than PF.

3.2. Analysis of Stress–Strain Curve and Damage Mode of Fiber-Influenced Filling Body

(1) Stress–strain relationship

Each set of typical specimens was chosen in order to analyze its stress–strain curve and to thoroughly explore the deformation process of each level of the filling body under a uniaxial compression load (see Figure 4). As shown in Figure 4, the damage process of a fiber-filled body that has been subjected to uniaxial compression and is both doped and undoped may be loosely separated into four stages: initial pore compaction (OA), linear elastic deformation (AB), plastic yielding (BC), and post damage (CD).

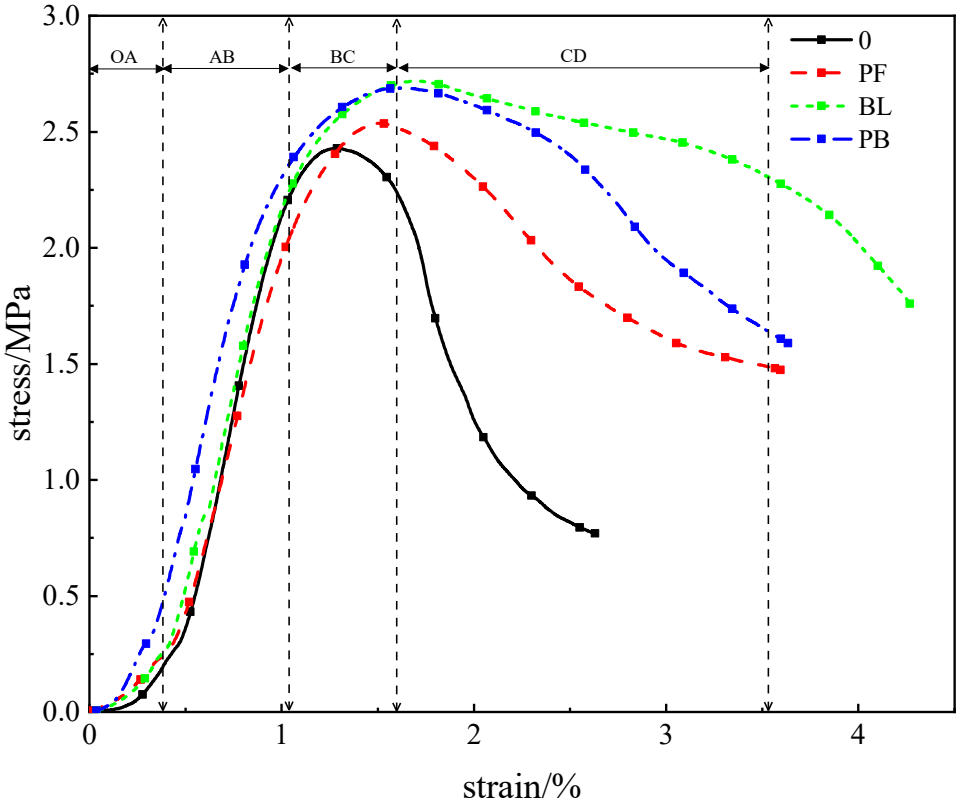


Figure 4. Stress–strain curves of fillers doped with different fibers.

The application of load in the OA section caused the initial pores inside CTB to compress. At this point, the curve showed a progressive "upward concave" development. This could be because the fiber mixing makes CTB more compact, fills the matrix's internal pores, and optimizes the material's initial microstructure, making the fiber-doped filler body less visible at this point in the compaction process. Figure 4 shows that the fiber-doped filling body's axial strain is lower at this stage than it is for the non-fiber filling body, which will advance to the next stage sooner [22].

As the load continues to be applied, CTB in the AB section changes from a discontinuous medium to a continuous medium. At this point, the curves of all the specimens exhibit a "linear" quick expansion. In Figure 4, it can be observed that the slope of the curve for the fiber-doped filler is higher than that of the fiber-free filler. This difference may be explained by the fact that the fiber doping increases the filler's modulus of elasticity, which in turn increases its strength and toughness [23,24].

As shown in Figure 4, the peak strength of the fiber-doped filled body was higher than that of the fiber-free body. The reason may be that the fiber can bear the main load at

the crack and alleviate the stress concentration phenomenon. In the BC section, the crack evolution activity inside the filled body accelerated in this stage, and cracks occasionally appeared on the specimen surface, accompanied by a small area of extended joints. The major load at the cracks may be carried by the fibers, which also alleviate the stress concentration at the fracture tip and transfer the stress to the nearby, uncracked areas. This successfully prevents crack development and growth and increases the overall strength of CTB.

The strength of the CTB gradually decreases, but it will not be reduced to zero in the CD section as the load continues to act. As a result, the internal structure of the CTB sustains significant damage, and several macroscopic cracks parallel to the load direction appear on its surface. As can be seen in Figure 4, the decline of the stress–strain curve of the fiber-doped filling body in the post-peak curve tends to be slower than that of the ordinary filling body. The analysis was performed because the structure of CTB, which is what is mostly causing the material's loss of strength, depends on the fiber. In the construction of CTB, fibers have a bridging role that can delay or prevent the shedding of the edge block expand the specimen's effective stress area and disperse the compressive stress uniformly, enhancing CTB stability [25].

(2) Destruction mode

In order to discuss the effects of incorporating different fibers on the macroscopic damage mechanism of the filler, the final damage pattern of each type of filler under uniaxial compressive loading needs to be analyzed (see Figure 5). As shown in Figure 5, there are notable differences between the final damage morphologies of the fiberless filled body and fiber-doped filled body. The fiberless filled body underwent uniaxial compression loading, which clearly caused brittle damage, as evidenced by the main cracks that extend through the specimen end face. These cracks have a "wide and long" morphology, and a sizable portion of the block body appeared to be peeling off along the main crack development area. This is because, during the curing process, the filling body will absorb some of the free water resulting from the cement's hydration reaction within the matrix. This will release a significant amount of heat and cause the water to evaporate within the matrix, causing the filling body to internally shrink and crack and creating a large number of initial pores. Loading the early primary pores close to the stress concentration phenomenon will cause the development of small cracks to occur faster and the continued expansion of when the load exceeds the peak strength, the crack development speed is accelerated, and the specimen surface forms the macroscopic main cracks visible to the naked eye. Comparing the PF filler's damage pattern to that of the fiber-free filler, it can be seen that under external loading, several main cracks parallel to the direction of loading manifest on the specimen's surface. These cracks are smaller in width and do not extend through the specimen's upper and lower end surfaces. The specimen surface almost does not seem to flake off the phenomenon, and when looking at the middle and both sides of the specimen, there are more minor cracks randomly distributed, forming a net-like structure. Overall, the group of filling body specimens can still maintain macro-stability until the end of the test. Its primary cause may be that the original pore space within the CTB under the continuous action of the external load gradually forms small cracks, which continuously extend and expand outward. When the crack extension meets the fiber, its generation and expansion rate is slowed, which reduces the length and width of the cracks' rate of growth. The stress concentration area inside the specimen will now be moved to additional weak areas as a result of the ongoing action of the external load. This will cause new, smaller, and denser microcracks to develop at random [11]. The distribution of cracks at the end of the specimen for BL and PB fillers is similar to that of the PF filler, which is primarily dominated by randomly distributed secondary cracks. The surface of the filler is almost free of through cracks, and the entire structure is macroscopically stable with a high residual strength.

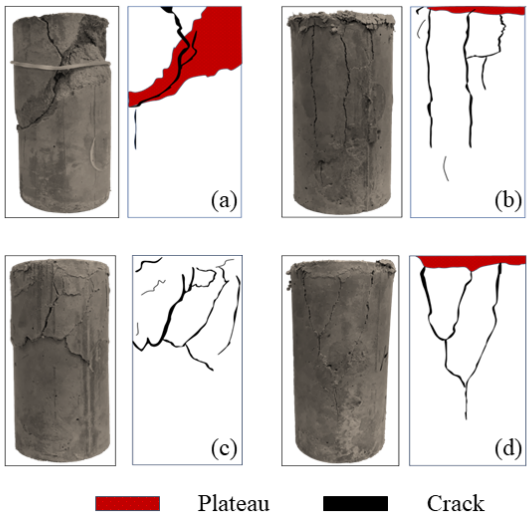


Figure 5. Damage pattern of different fiber-doped fillers; (**a**) 0; (**b**) PF; (**c**) BL; (**d**) PB.

Additionally, the secondary fractures on the surface of the BL filler are distinguished by their large width and small number, in contrast to the fracture shapes of PF and PB fillers, where the development of fractures parallel to the main load direction is more obvious. Overall, monoclinic shear damage is predominant. This phenomenon may be caused by the substantial, stiff modulus of elasticity of the glass fiber, which results in BL filling bodies with a high strength but low toughness. The overall appearance of the fissure also displays "wide and few" traits. The PB filling body has more destructive qualities than the PF and BL filling body groups due to its higher strength, greater toughness after the peak, and characteristically "fine and many" damaging fractures. As a result of the fibers' effective bridging and blocking properties, the development and expansion of fissures are effectively suppressed, which improves the filling body's integrity after peaking and increases its toughness. This optimization is extremely important for the filling body to support the air–sea zone downhole and prevent the subsidence of nearby rocks.

3.3. AE Characterisation

An AE (AE) event happens when an external loading damages a filled body and releases energy as elastic waves into the environment [26–28]. Existing research has demonstrated that when injured by external loads, the internal microfracture expansion and evolution patterns of filling body specimens generated under various conditions are not the same, and the ultimate damage modes are also noticeably different [29,30]. Therefore, based on the inherent relationship between the internal fracture evolution law and the filling body's AE signal parameters, this study examines the variations in the AE energy values of the filling body doped with various fibers during the uniaxial compression process and then identifies the mechanism of the fiber-affected fracture expansion.

The AE energy–stress–time connections for uniaxial compression of the various doped fiber-filled bodies are shown in Figure 6. According to Figure 6a, the AE event occurs early in the loading of the fiberless filling body, and the AE energy value exhibits a slight increasing trend. When the loading is applied close to its peak intensity, the AE energy increases to its maximum value, and as the loading enters the post-damage stage. The AE activity starts to decline, which is consistent with the AE energy's value gradually declining. The above phenomenon may be caused by the internal voids of the filling body being compacted at the early stages of loading, which produces a small amount of AE signal. However, when the stress is increased to be close to the peak intensity, the surface of the fiberless filling body appears to be macroscopically damaged in a large area, and the strain energy that has accumulated in the interior of the body is quickly released, which causes the AE signals.

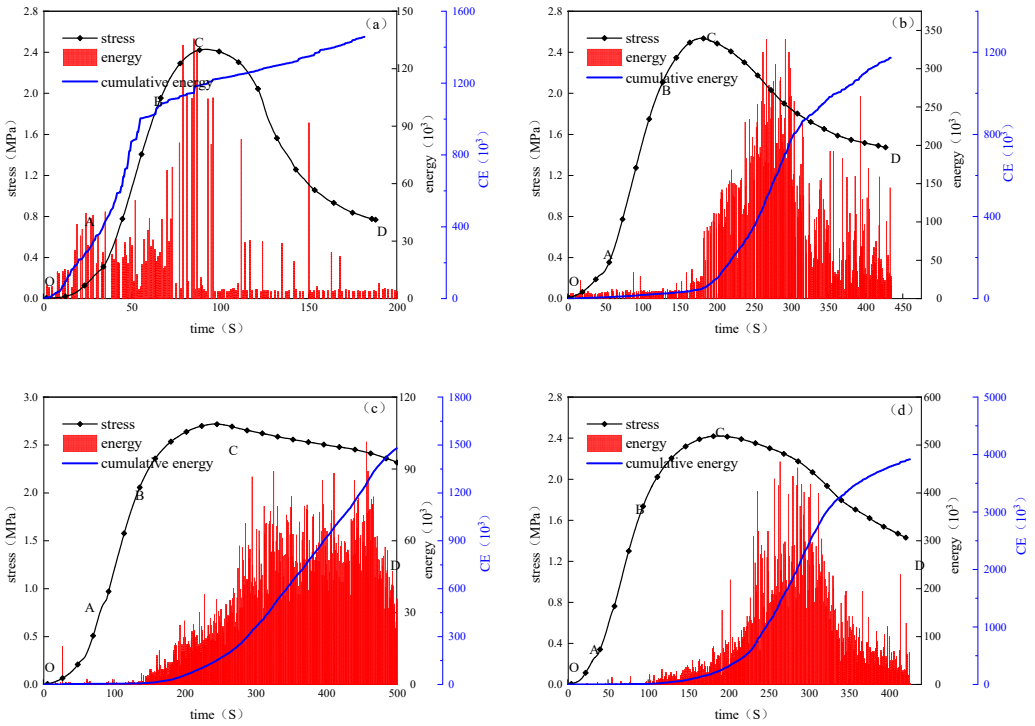


Figure 6. Energy–stress–time relationship of AE doped with different fiber fillers; (**a**) 0; (**b**) PF; (**c**) BL; (**d**) PB.

Furthermore, it can be seen from Figure 6b–d that the characteristics of the AE signals of the PF-, BL-, and PB-filled bodies and the fiber-free bodies are noticeably different. More specifically, the fiber-doped filled bodies hardly produce AE signals at the early stage of the load effect, and the AE signals appear sporadically until the stress approaches the yield strength. As the plastic begins to give, the AE signal strength rises progressively and the AE energy value increase as well, reaching its maximum value and remaining at a high level in the post-damage period. The above phenomenon is caused by two factors. First, the fiber enhances the microstructure of the filling body and reduces the quantity of primary pores. This lowers the event rate of the fiber-doped filling body in the OA region of the pores and lessens the possibility that an AE signal will be generated at this location. Secondly, in the post-damage stage, the strain energy accumulated within the fiber tends to become saturated. If the load continues to be applied, a small number of fibers dispersed within the matrix will be fatigue ruptured. This cannot stagnate crack sprouting, resulting in the emergence of many small cracks randomly. Therefore, the doped-fiber-filled body at this stage of the AE signals is unusually active and maintained at a high level for a long time.

In conclusion, fiberless filling bodies and PF, BL, and PB filling bodies exhibit observable differences in the change rule of the AE energy value over time during the uniaxial compression process. Additionally, based on the analysis of the damage pattern in the previous section, it is known that the change rule of AE energy value is intrinsically related to the damage morphology of the filling bodies, and as a result, an abnormal increase in the value of AE energy can be used as a precursor.

4. Damage Model Construction of the Filling Body Based on the AE Energy Value

Based on the findings of previous studies, it is clear that the dynamic evolution of internal fissures in doped and undoped fiber-filled bodies under uniaxial compression differs noticeably. Furthermore, the value of the AE energy is closely related to the evolution of the degree of damage to the material's internal fissures. Therefore, the development of a functional relationship between the filler dynamics parameter and the AE energy is necessary.

In this study, the filling body's degree of damage is assessed using the cumulative energy value of AE during the uniaxial compression process. The functional relationship between the cumulative energy of the AE and strain is built using loading time as the intermediary variable. The damage constitutive model of the doped and undoped fiber-filled body is built using the Lemaitre strain equivalence principle and the presumption that the filling body's microelemental strength obeys the Weibull distribution function [31,32]. By function fitting, the following relationship between the filling body's deformation and the loading time is known:

$$\varepsilon = kt + \varepsilon_0 \tag{1}$$

where ε is the specimen strain; k is the strain rate of the specimen; and ε_0 is the initial strain of the specimen, which can be derived through linear fitting of the test data.

Under uniaxial compression of the various doped fiber-filled bodies, the cumulative acoustic emission energy values were derived as a function of time by fitting the test data to an S-function with the time variable (see Figure 7).

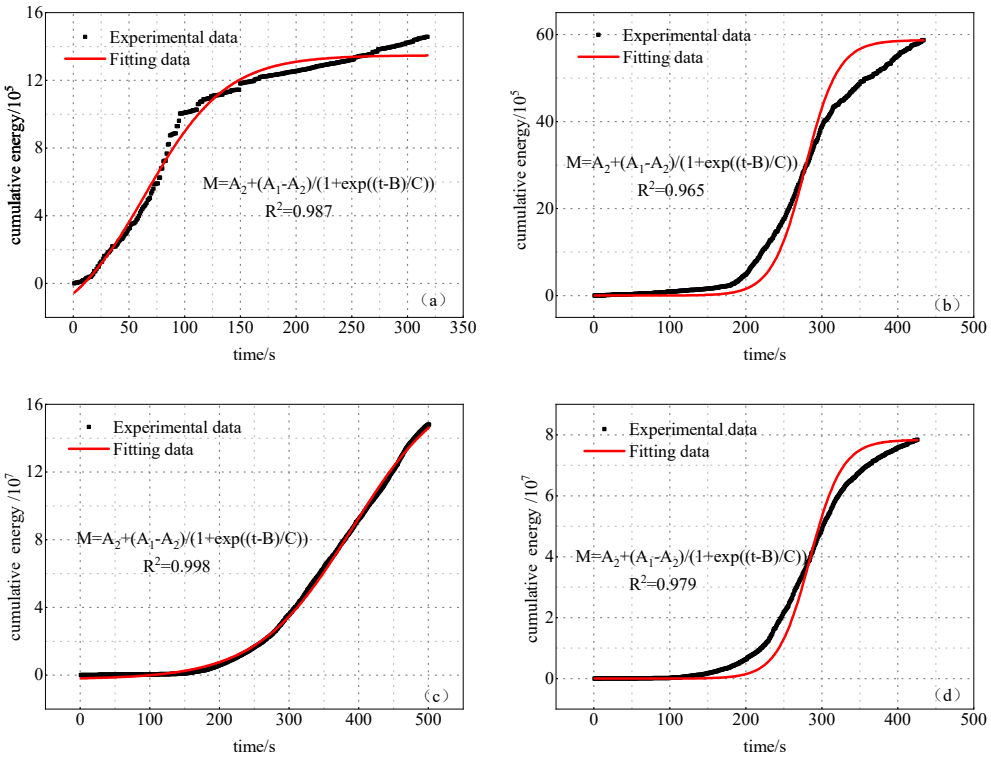


Figure 7. Doping of different fiber fillers M as a function of t; (**a**) 0; (**b**) PF; (**c**) BL; (**d**) PB.

According to Figure 7, the specimens doped with various fiber-filled bodies emit sound with a cumulative energy and time that follow the Boltzmann functional relationship [33,34]:

$$M = A_2 + \frac{A_1 - A_2}{\left[1 + \exp\left(\frac{t-B}{C}\right)\right]} \tag{2}$$

where M is the cumulative energy of the AE; A_1, A_2 are the minimum and maximum values of the cumulative AE energy, respectively; and the B, C values can be fitted from the test data.

The coupled Equations (1) and (2) can establish the cumulative AE energy value of the four types of filler specimens M as a function of strain:

$$M = A_2 + \frac{A_1 - A_2}{1 + \exp\left[\frac{(\varepsilon-\varepsilon_0)-KB}{KC}\right]} \tag{3}$$

Based on the Lemaitre strain equivalence assumption [31], the state of damage and breakage of the tailing sand-cemented fill can be expressed by the effective stresses:

$$\sigma = E\varepsilon\ (1 - D) \tag{4}$$

where σ is the effective stress, E is the elastic modulus of CTB, ε is the strain, and D is the damage variable.

Since CTB is composed of cement and tailing sand, which belongs to a kind of rock-like material, and based on the literature [32], it is assumed that the microelement strength of CTB obeys the Weibull distribution:

$$\Phi(\varepsilon) = \frac{m}{\alpha}\varepsilon^{m-1}\exp\left[-\frac{\varepsilon^m}{\alpha}\right] \tag{5}$$

where α, m are Weibull distribution covariates, which are related to the homogeneity of CTB.

The damage variable D is related to the probability density of the microelement destruction as follows [35,36]:

$$\frac{dD}{d\varepsilon} = \Phi(\varepsilon) \tag{6}$$

Equations (5) and (6) and their simplification give the damage variable as:

$$D = \int_0^{\varepsilon} \Phi(\varepsilon)\mathrm{d}\varepsilon = 1 - \exp\left[-\frac{\varepsilon^m}{\alpha}\right] \tag{7}$$

Substituting Equation (7) into Equation (4) yields:

$$\sigma = E\varepsilon\ (1 - D) = E\varepsilon\exp\left[-\frac{\varepsilon^m}{\alpha}\right] \tag{8}$$

Based on the stress–strain relationship of CTB, it can be concluded that there are the following boundary conditions:

$$\begin{cases} \sigma = 0, \varepsilon = 0 \\ \sigma = \sigma_p, \varepsilon = \varepsilon_p \\ \sigma = \sigma_p, \frac{d\sigma}{d\varepsilon} = 0 \\ \left.\frac{d\sigma}{d\varepsilon}\right|_{D=0} = E \end{cases} \tag{9}$$

where σ_p is the peak intensity and ε_p is the peak strain.

When $\sigma = \sigma_p, \varepsilon = \varepsilon_p$, substituting them into Equation (8) yields:

$$\sigma_p = E\varepsilon_P\exp\left[-\frac{{\varepsilon_p}^m}{\alpha}\right] \tag{10}$$

Collating Equation (10) gives:

$$\exp\left[-\frac{{\varepsilon_p}^m}{\alpha}\right] = \frac{\sigma_p}{\mathrm{E}\varepsilon_p} \tag{11}$$

$$\frac{{\varepsilon_p}^m}{\alpha} = \ln E\varepsilon_P - \ln\sigma_p \tag{12}$$

When $\sigma = \sigma_p, \frac{d\sigma}{d\varepsilon} = 0$, substituting them into Equation (8) yields:

$$\frac{d\sigma}{d\varepsilon} = Eexp\left[-\frac{{\varepsilon_p}^m}{\alpha}\right] + E\varepsilon_p\exp\left[-\frac{{\varepsilon_p}^m}{\alpha}\right]\left(-\frac{m\varepsilon^{m-1}}{\alpha}\right) = 0 \tag{13}$$

Collating Equation (13) and combining Equations (11) and (12) yields:

$$m = \frac{1}{\ln E\varepsilon_P - \ln \sigma_p} \tag{14}$$

$$\alpha = m{\varepsilon_p}^m \tag{15}$$

Substituting the values of Equations m and α into Equations (7) and (8) yields the strain as a function of the stress and damage variables as follows:

$$\sigma = E\varepsilon \exp\left[-\frac{\varepsilon^m}{m{\varepsilon_p}^m}\right] \tag{16}$$

$$D = 1 - \exp\left[-\frac{\varepsilon^m}{m{\varepsilon_p}^m}\right] \tag{17}$$

Collating Equation (3) yields an expression for ε in terms of the M-values as follows:

$$\varepsilon = KC \times LN\frac{A_1 - M}{M - A_2} + KB + \varepsilon_0 \tag{18}$$

The couplings (16)–(18) lead to the stress σ and the damage variable D as a function of M as follows:

$$\sigma = E\left(KC \times LN\frac{A_1 - M}{M - A_2} + KB + \varepsilon_0\right) \exp\left[-\frac{\left(KC \times LN\frac{A_1 - M}{M - A_2} + KB + \varepsilon_0\right)^m}{m{\varepsilon_p}^m}\right] \tag{19}$$

$$D = 1 - \exp\left[-\frac{\left(KC * LN\frac{A_1 - M}{M - A_2} + KB + \varepsilon_0\right)^m}{m{\varepsilon_p}^m}\right] \tag{20}$$

Table 4 displays the Weibull distribution's parameters as well as the fitting variables used in the previous calculation.

Table 4. Weibull distribution and fitting parameters.

Fiber Type	Weibull Distribution Parametric		Fit Parameter					
	m	α	A_1	A_2	B	C	K	ε_0
0	1.443	0.00268	−295,745	1,348,439.51	64.72	36.28	4.0×10^5	2×10^4
PF	1.708	0.0013099	−29,241	5,868,201.12	278.08	21.65	4.0×10^5	1×10^4
BL	1.412	0.00448	−2,426,160	1.7542×10^8	390.36	67.79	4.0×10^5	4×10^4
PB	2.336	0.0001556	−302,522	7.83514×10^7	284.26	21.25	4.0×10^5	4×10^4

5. Model Validation and Discussion

In Figures 8 and 9, one can see the relationship between the experimental and model data for the cumulative energy–stress and cumulative energy–damage variables. This relationship is obtained by replacing the experimentally obtained data with the corresponding damage equations derived above. As seen in Figure 8a, the experimental curves of the cumulative energy–stress of AE from the fiberless filler are slightly different from the model curves, and they are primarily reflected in the pre-peak stage. This difference may be caused by the filler's poor stability of microfracture emergence and development under early loading, which causes the enhanced dispersion of AE signals and the discrepancy between the model results. The experimental curves of the cumulative AE energy versus stress for the PF, BL, and PB fillers, as seen in Figure 8b–d, show a high degree of agreement with the model curves, particularly in the pre-peak phase, which is almost exactly

matched. This phenomenon differs noticeably from that of the fiberless fillers, however. The pre-peak stage may be the reason for this, because the fibers can effectively prevent the growth and expansion of microcracks, making the filling body's microelement destruction more uniform and weakening the AE signal dispersion. As a result, the model results and experimental results agree well.

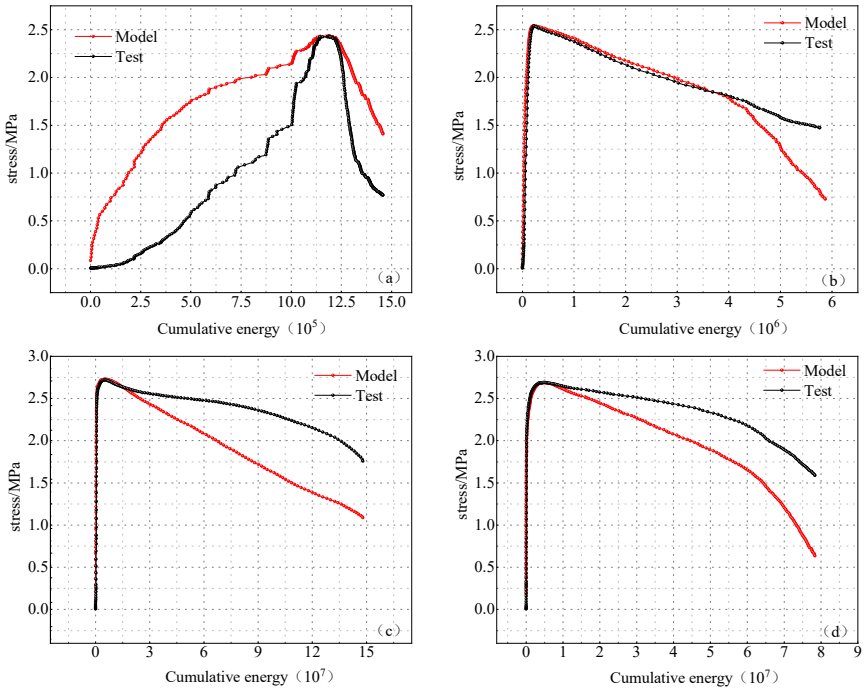


Figure 8. Analysis of experimental and modelling results of AE cumulative energy versus stress relationship; (**a**) 0; (**b**) JBX; (**c**) BL; (**d**) HB.

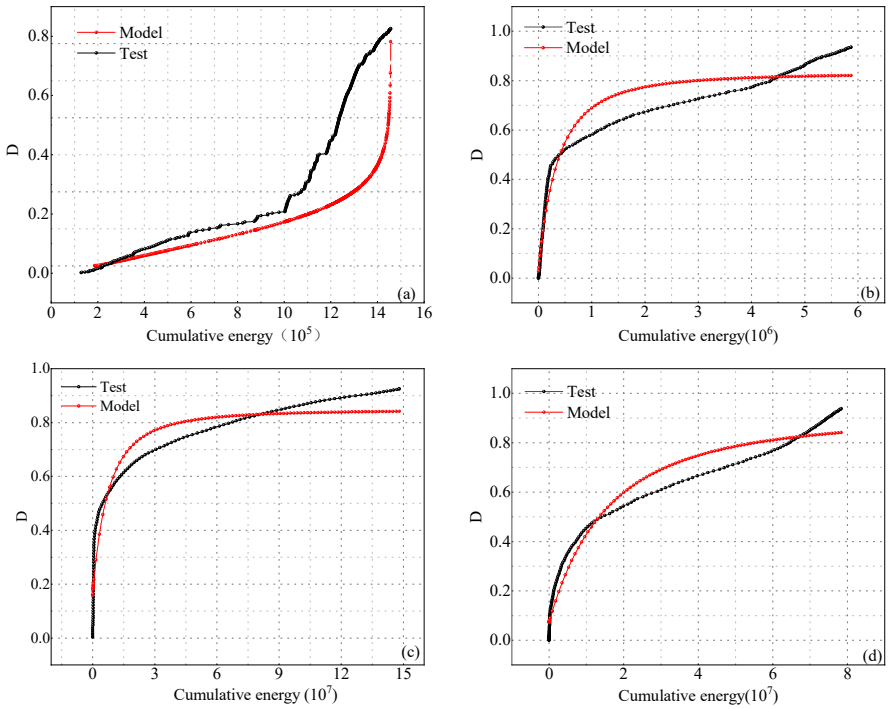


Figure 9. Analysis of experimental and modelling results of the relationship between cumulative AE energy and damage; (**a**) 0; (**b**) JBX; (**c**) BL; (**d**) HB.

Additionally, it should be noted that the PF, BL, and PB fillers do not exhibit a significant increase in cumulative AE energy along with a significant increase in intensity; a phenomenon that differs significantly from that of the fiberless fillers, thereby laterally indicating that the fiber-doped fillers do not have an active AE signal in the pre-peak phase, which is consistent with the earlier findings. This phenomenon may be caused by the fact that the majority of the mechanical energy generated by the external load is transformed into the internal energy of the filling body and the elastic strain energy of the fibers, leaving only a small amount of mechanical energy to dissipate along with the filling body's micrometric destruction. The experimental curves of the cumulative AE energy-damage variables for the four fillers in Figure 9 reveal a pattern that is comparable to the predicted curves, which is generally in excellent agreement when compared to Figure 8.

After the aforementioned checks, it is clear that the damage model established in this paper, with time 't' acting as the intermediate variable between AE cumulative energy 'M' and stress, as well as between 'M' and the damage variable 'D', differs slightly from the experimental data but overall has a high degree of agreement. As a result, it is believed that the damage eigenmodel established in this paper is reasonable.

6. Conclusions

(1) The uniaxial compressive strength of the filling body can be significantly enhanced by fiber doping. In comparison to the fiber-free body, the uniaxial compressive strengths of the PF-, BL-, and PB-doped filling bodies increased, by 6.69%, 13.81%, and 10.04%, respectively, with the BL having the greatest enhancement effect.

(2) The four stages of the filler's loading curves under uniaxial compression loading are pore compaction, linear elastic deformation, plastic yielding, and post-destruction. When a filling body is fiber-free, it can macrofracture through the end face, causing destabilization damage and the local appearance of block spalling. In contrast, when a filling body is doped with PF, BL, or PB, it primarily exhibits smaller and more densely distributed microfractures that are dominant throughout the specimen as a whole, preserving its macroscopic stability.

(3) The AE of the fiber-free body is more active before the peak point and is relatively flat in the late damage stage, whereas the AE energy values of the fiber-doped body start to surge after the peak point and continue to be at a high level. The AE energy values of the specimens doped with different fiber-filled bodies vary greatly in different loading stages.

(4) By merging the Weibull distribution function assumption with the strain equivalency concept, the damage model of the AE cumulative energy, stress, and damage variables was developed. Based on the fitted functional relationship between the AE cumulative energy, strain, and time, the functional relationship between the AE cumulative energy and the strain of the various doped fiber fillers was established.

Author Contributions: C.Z.: experimental supervision, conceptualization, methodology; X.S.: experimental design, data processing, writing; Y.F.: conceptualization, methodology, review of first draft. D.L.: experimental guidance, methodology; W.S.: data processing, experiments, software; W.Z.: laboratory management, coordination, and cooperation. All authors have read and agreed to the published version of the manuscript.

Funding: This study was funded by National Natural Science Foundation of China under Grant No. [51464015].

Data Availability Statement: The datasets used and/or analyzed during the current study are available from the corresponding author upon reasonable request.

Conflicts of Interest: No conflict of interest exit in the submission of this manuscript, and manuscript has been approved by all authors for publication. The work described herein was original research that has not been published previously and is not under consideration for publication elsewhere, in whole or in part. All the authors have approved the manuscript that is enclosed.

References

1. Huynh, L.; Beattie, D.A.; Fornasiero, D.; Ralston, J. Effect of polyphosphate and naphthalene sulfonate ormaldehyde condensate on the rheological properties of dewatered tailings and cemented paste backfill. *Miner. Eng.* **2006**, *19*, 28–36. [CrossRef]
2. Yilmaz, E.; Belem, T.; Benzaazoua, M. Specimen size effect on strength behavior of cemented paste backfills subjected to different placement conditions. *Eng. Geol.* **2015**, *185*, 52–62. [CrossRef]
3. Qi, C.; Fourie, A. Cemented paste backfill for mineral tailings management: Review and future perspectives. *Miner. Eng.* **2019**, *144*, 106025. [CrossRef]
4. Yin, S.H.; Cao, Y.; Wu, A.X.; Hou, Y.X.; Bai, L.J. Study on Mechanics and Flow Behavior of Glass Fiber reinforced Cemented Sulfur Tailings Backfill. *Mater. Rep.* **2023**, *37*, 246–252.
5. Li, Y.; Bian, Y.; Liu, C. Damage and failure mechanism of basalt fiber-reinforced gangue-cemented backfill under uniaxial compression. *Constr. Build. Mater.* **2023**, *400*, 132872. [CrossRef]
6. Feng, G.R.; Xie, W.S.; Guo, Y.X.; Guo, J.; Ran, H.Y.; Zhao, Y.H. Effect of early load on mechanical properties and damage of cemented gangue backfill. *Chin. J. Rock Mech. Eng.* **2022**, *41*, 775–784.
7. Hua, X.Z.; Chang, G.F.; Liu, X.; Yang, K.; Chen, D.H.; Li, C.; Wang, E.Q. Strength evolution law and acoustic-emission characteristics of multi-source coal-based filling body of solid wastes. *Chin. J. Rock Mech. Eng.* **2022**, *41*, 1536–1551.
8. Cao, S.; Yilmaz, E.; Song, W. Fiber type effect on strength, toughness and microstructure of early age cemented tailings backfill. *Constr. Build. Mater.* **2019**, *223*, 44–54. [CrossRef]
9. Chen, X.; Shi, X.; Zhou, J.; Yu, Z. Influence of polypropylene fiber reinforcement on tensile behavior and failure mode of tailings cemented paste backfill. *IEEE Access* **2019**, *7*, 69015–69026. [CrossRef]
10. Xue, G.; Yilmaz, E.; Song, W.; Cao, S. Fiber length effect on strength properties of polypropylene fiber reinforced cemented tailings backfill specimens with different sizes. *Constr. Build. Mater.* **2020**, *241*, 118113. [CrossRef]
11. Zhao, K.; Song, Y.F.; Yu, X.; Zhou, Y.; Yang, Y.J.; Wang, J.Q. Study on early mechanical properties and damage constitutive model of tailing-cemented backfill with different fibers. *Chin. J. Rock Mech. Eng.* **2022**, *41*, 282–291.
12. Ruan, Z.E.; Wu, A.X.; Fu, H.; Wang, S.Y. Influence mechanism of straw fiber on uniaxial compressive strength cemented paste backfill body of sulfur-bearing tailings. *J. Cent. South Univ. (Sci. Technol.)* **2023**, *54*, 837–848.
13. Song, X.; Dong, Z.; Hao, Y.; Wang, S.; Li, J.; Yuan, Q. Study on mechanical properties and damage characteristics of rice straw fiber-reinforced cemented tailings backfill based on energy evolution. *Environ. Sci. Pollut. Res.* **2023**, *30*, 45295–45314. [CrossRef] [PubMed]
14. Wang, J.; Fu, J.; Song, W.; Zhang, Y.; Wang, Y. Mechanical behavior, acoustic emission properties and damage evolution of cemented paste backfill considering structural feature. *Constr. Build. Mater.* **2020**, *261*, 119958. [CrossRef]
15. Sun, K.; Zhang, J.; He, M.; Li, M.; Wang, C.; Feng, W.; Li, F. Mechanical properties and damage evolution characteristics based on the acoustic emission of gangue and high-water-content materials based cemented paste backfill. *Constr. Build. Mater.* **2023**, *395*, 132324. [CrossRef]
16. Cheng, A.; Zhou, Y.; Chen, G.; Huang, S.; Ye, Z. Acoustic emission characteristics and fracture mechanism of cemented tailings backfill under uniaxial compression: Experimental and numerical study. *Environ. Sci. Pollut. Res.* **2023**, *30*, 55143–55157. [CrossRef] [PubMed]
17. Xia, Y.; Lu, A.H. Analysis of the mechanical properties and damage characteristics of continuously graded high-strength cemented backfill. *J. Min. Strat. Control Eng.* **2023**, *5*, 013037.
18. Zhao, K.; Wu, J.; Yan, Y.J.; Zhou, Y.; Yang, J.; He, Z.W. Multi-scale characteristics of crack evolution of cemented tailings backfill. *Chin. J. Rock Mech. Eng.* **2022**, *41*, 1626–1636.
19. Zhao, K.; He, Z.W.; Yan, Y.J.; Yu, X.; Song, Y.F.; Yang, J. Microscopic failure mechanism of fiber reinforced ultra-fine tailings backfill. *Chin. J. Rock Mech. Eng.* **2022**, *41*, 3010–3020.
20. Yin, S.; Zhou, Y.; Chen, X.; Li, G. A new acoustic emission characteristic parameter can be utilized to evaluate the failure of cemented paste backfill and rock combination. *Constr. Build. Mater.* **2023**, *392*, 132017. [CrossRef]
21. Zhao, K.; Liu, Z.; Zeng, P.; Gong, C.; Li, Y. Fracture process analysis and acoustic emission response of cemented tailings backfill with different sizes under uniaxial compression. *Materials* **2022**, *15*, 8038. [CrossRef] [PubMed]
22. He, Z.W. *Macroscopic and Mesoscopic Trans-Scale Failure Mechanism in Polyacrylonitrile Fiber Reinforced Cement Backfill*; Jiang Xi University of Science and Technology: Ganzhou, China, 2023.
23. Gao, B.; Cao, S.; Yilmaz, E. Effect of content and length of polypropylene fibers on strength and microstructure of cementitious tailings-waste rock fill. *Minerals* **2023**, *13*, 142. [CrossRef]
24. Xue, X.; Gu, Y.; Zhang, X.; Wu, S.; Sun, P.; Cui, J.; Wang, X. Mechanical behavior and microscopic mechanism of fiber reinforced coarse aggregate cemented backfill. *Constr. Build. Mater.* **2023**, *366*, 130093. [CrossRef]
25. Zhao, K.; Zhao, K.; Yan, Y.; Yang, J.; Wu, J.; Lai, Y.; Liu, L.; Zeng, X. Influence of different fibers on compressive toughness and damage of early age cemented tailings backfill. *Environ. Sci. Pollut. Res.* **2023**, *30*, 37449–37461. [CrossRef] [PubMed]
26. Ohtsu, M. The history and development of acoustic emission in concrete engineering. *Mag. Concr. Res.* **1996**, *48*, 321–330. [CrossRef]
27. Sagar, R.V.; Prasad, B.K.R. A review of recent developments in parametric based acoustic emission techniques applied to concrete structures. *Nondestruct. Test. Eval.* **2012**, *27*, 47–68. [CrossRef]

28. Behnia, A.; Chai, H.K.; Shiotani, T. Advanced structural health monitoring of concrete structures with the aid of acoustic emission. *Constr. Build. Mater.* **2014**, *65*, 282–302. [CrossRef]
29. Prem, P.R.; Verma, M.; Ambily, P.S. Damage characterization of reinforced concrete beams under different failure modes using acoustic emission. *Structures* **2021**, *30*, 174–187. [CrossRef]
30. Xu, X.D.; Sun, G.H.; Yao, X.L.; Liang, X.J.; Shao, L.H. A cusp catastrophe warning model for instability of backfill based on energy dissipation and release. *Rock Soil Mech.* **2020**, *41*, 3003–3012.
31. Lemaitre, J. A continuous damage mechanics model for ductile fracture. *J. Eng. Mater. Technol.* **1985**, *107*, 83–89. [CrossRef]
32. Tang, C.A.; Wang, S.H.; Fu, Y.F. *Numerical Tests of Rock Fracture Processes*; Science Publishers: Beijing, China, 2003.
33. Lai, Y.; Zhao, K.; Yan, Y.; Yang, J.; Wu, J.; Ao, W.; Guo, L. Damage study of fiber-doped superfine tailings cemented backfill based on acoustic emission cumulative ringing count. *J. Mater. Sci.* **2022**, *57*, 11612–11629. [CrossRef]
34. Wang, X.J.; Zhang, H.; Chen, Q.L.; Zeng, Q.; Liu, J. Acoustic emission characteristics and damage model of limestone loading with different rockburst tendencies. *Chin. J. Rock Mech. Eng.* **2022**, *41*, 1373–1383.
35. Ohtsu, M. Acoustic emission characteristics in concrete and diagnostic applications. *J. Acoust. Emiss.* **1987**, *6*, 99–108.
36. Wu, X.Z.; Liu, J.W.; Liu, X.X.; Zhao, K.; Zhang, Y.B. Study on the coupled relationship between AE accumulative ring-down count and damage constitutive model of rock. *J. Min. Saf. Eng.* **2015**, *32*, 28–34+41.

Disclaimer/Publisher's Note: The statements, opinions and data contained in all publications are solely those of the individual author(s) and contributor(s) and not of MDPI and/or the editor(s). MDPI and/or the editor(s) disclaim responsibility for any injury to people or property resulting from any ideas, methods, instructions or products referred to in the content.